# Dynamical motion of an oblate shaped particle exposed to an acoustic standing wave in a microchannel

S. Z. Hoque ⓘ, K. Bhattacharyya, and A. K. Sen ⓘ*
*Fluid Systems Laboratory, Department of Mechanical Engineering,*
*Indian Institute of Technology Madras, Chennai 600036, India*

The nonlinear effects induced on a nonspherical object exposed to an acoustic standing wave offer acoustic radiation force and torque, resulting in the dynamical motion of the object. Here, we study the translational and rotational motion of an oblate shaped particle exposed to standing bulk acoustic waves in a microchannel using numerical simulations. Acoustic pressure and velocity fields are obtained from a numerical model, and a perfectly matched layer boundary condition is used to simulate the particle dynamics. A systematic parametric study is carried out to understand the effects of initial orientation, aspect ratio, size, and initial location of the particle on the translational and rotational motion, by considering the acoustic streaming effects. In this paper, we reveal that the particle undergoes rotation to minimize the acoustic radiation torque potential when the minor axis of the particle is not in line with the acoustic pressure wave direction. We find that the direction of rotation changes from anticlockwise to clockwise beyond a critical aspect ratio of the particle. The location of maximum torque and consequently particle rotation shift closer to the pressure node with increased particle size for a constant aspect ratio. Our results show that a particle positioned closer to the pressure node rapidly rotates, attributed to a sharp increase in acoustic radiation torque acting on it owing to a higher torque potential. In this paper, we shed light on the dynamical motion of an oblate shaped particle exposed to acoustic standing waves which may be relevant in understanding the dynamics of an elongated micro-organism or biological cells.

## I. INTRODUCTION

Over the past decades, the field of acoustofluidics has gained momentum through experimental, numerical, and theoretical developments that focus on the manipulation of micro-objects inside a microchannel [1]. When a micro-object suspended in a fluid medium is exposed to bulk acoustic waves, the object experiences mainly two acoustic effects. First, an acoustic radiation force acts on the object, which occurs due to the scattering of the acoustic wave from its surface. The primary radiation force acting on the particle depends on the density and compressibility difference between the object and the suspending fluid [2]. Second, the particle experiences a drag force due to the acoustic streaming-induced velocity field, which is approximated using the Stokes equation. The effect of the acoustic radiation force on a spherical particle is well studied in the literature [3–7]. In a seminal work, an expression for the acoustic radiation force acting on a rigid sphere in an ideal fluid was derived [8]. Subsequently, this expression was modified by Hasegawa and Yosioka [4] including the compressibility of the particle. Further, Gor'kov [9] proposed an expression for the acoustic force potential based on the kinetic and potential energies of the acoustic wave. Later,

---

*Corresponding author: ashis@iitm.ac.in

the acoustic radiation force acting on a spherical particle in a viscous fluid was investigated [10]. Interaction between multiple particles exposed to acoustic waves can give rise to the interparticle radiation force which has also been studied [11].

Several theoretical studies have been presented in the literature for calculating the acoustic radiation force and torque acting on a nonspherical particle. A generalized expression for primary acoustic radiation force for ellipsoids exposed to the bulk acoustic standing wave was reported [12]. The primary acoustic radiation force and acoustic radiation torque acting on a prolate shaped particle under the bulk acoustic standing wave were presented [13]. Subsequently, the acoustic radiation force and moment were calculated and it was shown that previously reported analytical solutions fail to approximate the radiation force and torque [14]. This is because since the particle shape affects the scattered acoustic field, it is difficult to derive a generalized analytical expression of the acoustic potential for any arbitrary shape particle. Recently, numerical simulations have been attempted for modeling acoustic radiation forces and torques acting on an arbitrary shape particle. A steady-state numerical model was proposed based on the boundary element model for calculating the acoustic radiation force and torque acting on a nonspherical particle [15]. A literature review suggests that although the acoustic radiation force and torque acting on nonspherical particles have been exclusively studied, investigation of the dynamical motion of such particles has not received much attention.

Understanding the dynamics of nonspherical particles inside microchambers exposed to ultrasonic waves may lead to potential microrobotics applications in the fields of science, engineering, biology, and medicine [16]. Precise control of the dynamical behavior of particles through the control of acoustic waves will have great relevance in microrobotic manipulations [17–19]. The formation of particle clusters using acoustic waves could enable a controlled analysis of biological particles [20]. Similarly, the superposition of two orthogonal standing waves can create a two-dimensional array for acoustic trapping of microparticles [21]. It is possible to orient a nonspherical particle in a specific direction due to the acoustic radiation torque acting on a particle [20]. A time-harmonic device model was developed to simulate the acoustofluidics device and calculate the acoustic pressure and velocity fields inside a microchannel [22]. Further, the pressure and velocity fields were used to calculate the radiation force and torque on a complex particle, viz., red blood cell, and disk shaped particle. A perfectly matched layer (PML) based method was proposed to study the dynamical motion of a nonspherical particle under the bulk acoustic wave, wherein the acoustic torque acting on an arbitrary shape particle exposed to an orthogonal acoustic standing wave was numerically approximated [23]. In the case of two phase-shifted orthogonal standing waves, the resulting streaming pattern around the suspended particle created a nonzero acoustic viscous torque that induced particle rotation. Rotation of spherical particles due to acoustic streaming was shown under two orthogonal standing waves [24]. Recently, the concept of torque potential was introduced, similar to the Gor'kov force potential [9], to characterize the rotational motion of a prolate shaped particle exposed to an acoustic wave [25]. The rotation of nonspherical glass fiber particles under two orthogonal standing waves was experimentally studied [26]. It was found that the direction and velocity of rotation can be varied by changing the amplitude of the two orthogonal standing waves. Rotation and translation of disk shaped alumina microparticles in a one-dimensional (1D) bulk acoustic standing wave were experimentally investigated [27], and a numerical model was validated against the experimental findings. An experimental study showed that nonspherical particles in a microchannel can be oriented as per the requirement for different applications such as field of flow and imaging cytometry, by putting transducers at different angles and positions [28]. In this study, the controlled orientation of red blood cells inside an acoustofluidic chip was presented.

In view of the above literature, we find that the fundamental understanding of the dynamical behavior of an arbitrary shape particle exposed to bulk acoustic waves has not received much attention. Although it has been shown that a nonspherical particle tends to rotate when exposed to a bulk acoustic standing wave, the rotational dynamics such as the direction of rotation and orientation dependency is not well understood. Here, we investigate the translational and rotational motion of an oblate shaped particle when exposed to a bulk acoustic standing wave. We extended

an existing numerical model [29] and modified the device modeling approach through multiphysics coupling for computing the acoustic pressure and streaming velocity field. Further, the computed pressure and velocity field is utilized to calculate the acoustic radiation force and torque acting on an oblate shaped particle to explain the translational and rotational motion of an oblate shaped particle. We perform a parametric study to elucidate the translational and rotational dynamics of the particle by varying the initial orientation, aspect ratio, initial position, and particle volume.

## II. NUMERICAL MODEL

### A. Acoustic radiation force and torque

The governing equations used to estimate the acoustic radiation force and torque acting on the particle are discussed in this section. The perturbation theory is employed to derive the first-order and second-order acoustic fields considering a compressible and Newtonian fluid [30]. A three-dimensional model is used to calculate the acoustic radiation force acting on a particle by considering the incident and scattering waves and integrating the time-averaged acoustic fields using the tensor integral method [31]. For nonreflecting boundary conditions of the acoustic wave from the walls, perfectly matched layers (PML) surrounding the particle are used. Following the work of Hahn *et al.*, the PML domain is chosen based on the particle size instead of the wavelength [22]. Hahn *et al.* explained that the acoustic domain for the fluid and the suspended particle could be modeled using either an acoustic structure interaction module or two pressure acoustic modules [22]. The PML layer is used to avoid the backscattering at the domain boundaries to nullify the effects of the wall in the present simulation. The size of the PML layer is chosen based on the particle size which helps in reducing the computational time. In the present case, the frequency domain is used to calculate the acoustic radiation force and torque and therefore the size or thickness of the PML domain will not alter the acoustic scattered pressure field [32].

We consider homogenous isentropic fluid with thermodynamic equilibrium as an unperturbed or zeroth-order state. Now, using the standard perturbation terms up to the second order, the pressure ($p$), density ($\rho_f$) and velocity (**v**) fields can be expressed as

$$p = p_0 + p_1 + p_2 + \cdots, \tag{1}$$

$$\rho_f = \rho_0 + \rho_1 + i + \cdots, \tag{2}$$

$$\mathbf{v} = 0 + \mathbf{v}_1 + \mathbf{v}_2 + \cdots. \tag{3}$$

Here, 0, 1, and 2 are the zeroth-order, first-order, and second-order perturbations, respectively. For inviscid flow, the perturbed pressure fields are obtained as

$$p_1 = -\rho_0 \partial_t \phi_1, \tag{4}$$

$$p_2 = \frac{\rho_0}{2c_0^2}(\partial_t \phi_1)^2 - \frac{\rho_0}{2}|v_1|^2. \tag{5}$$

Considering the time variation to be periodic, the time average of the first-order field leads to $\langle p_1 \rangle = 0$, and only the time-averaged second-order field remains. The average force acting on a particle is equal to that of momentum flux through the surface of the particle, which is given as [22]

$$\mathbf{F_r}.n_i = -\int_{\partial V}[p_2 + \rho_0 \langle v_{1,i} v_{1,j} \rangle]n_j dA, \tag{6}$$

$$\mathbf{F_r}.n_i = -\int_{\partial V}\left[\left\{-\frac{\rho_0}{2}\langle |v_1|^2 \rangle + \frac{\rho_0}{2c_0^2}\langle (\partial_t \phi_1) \rangle^2\right\} + \rho_0 \langle v_{1,i} v_{1,j} \rangle\right]n_j dA. \tag{7}$$

Similarly, the acoustic radiation torque can be obtained using the following expression [22]:

$$\mathbf{T_r}.n_i = -\int_{\partial V} \epsilon_{ijk} r_j \left[ \left\{ -\frac{\rho_0}{2}\langle|v_1|^2\rangle + \frac{\rho_0}{2c_0^2}\langle(\partial_t \phi_1)\rangle^2 \right\} + \rho_0\langle v_{1,i}v_{1,j}\rangle \right] n_j dA. \tag{8}$$

Here, $\epsilon_{ijk}$ is the Levi-Civita symbol and $r_j$ is the displacement vector from the center of mass of the particle to that of the surface of the particle. Here, $n_j$ is the unit normal vector pointing at the particle surface. The tensor integral is carried out over the surface $\partial V$ of the particle.

## B. Acoustic torque potential

Simlar to the acoustic force potential or Gor'kov potential, the acoustic torque potential can be defined in order to better understand the rotational motion of the particle when exposed to bulk acoustic waves [9]. The torque acting on a spheroidal particle exposed to a plane standing wave is given by $T_r = (\tau_0)/2\sin(2\theta)$, where $\tau_0$ is defined as the characteristic radiation torque [25]. The mathematical definition of the characteristic radiation torque is given as $\tau_0 = VE_{ac}Q_{rad}$, where $V$ is the volume of the particle, $E_{ac}$ is the energy density of the wave, and $Q_{rad}$ is the dimensionless radiation torque efficiency [25]. The work done by the radiation torque to move the particle from $\theta = \frac{\pi}{2}$ to $\theta = \theta_k$ is obtained as

$$W = \int_{\frac{\pi}{2}}^{\theta_k} T_r(\theta)d\theta = -\frac{\tau_0}{2}\cos^2\theta_k. \tag{9}$$

Therefore, the total potential energy associated with the radiation torque is given by

$$\Delta U = U(\theta_k) - U\left(\frac{\pi}{2}\right) = -W = \frac{\tau_0}{2}\cos^2\theta_k. \tag{10}$$

The minimum of the torque potential energy is obtained for the angle $\theta_k = \frac{\pi}{2}$, i.e., when the major axis of the particle is perpendicular to the wave direction—the condition corresponds to the stable equilibrium position. The torque potential becomes maximum for $\theta_k = 0^0$, i.e., when the major axis of the particle is aligned with the standing wave direction. For $\theta_k = 0°$, although the particle experiences zero acoustic radiation torque, the particle is in an unstable equilibrium condition and starts rotating due to the maximum torque potential. The acoustic torque potential elucidates the rotational equilibrium position of the particle, which cannot be explained only through the acoustic radiation torque.

## C. Device model—pressure and velocity fields

A bulk acoustofluidics device typically consists of solid substrates, viz., a transducer, a silicon substrate, and a glass substrate, with the silicon and glass substrates bonded to each other using anodic bonding [33–38]. The schematic of an acoustofluidics device with a straight channel is shown in Fig. 1. The half-wave pressure node formation inside the microchannel is shown in Fig. 1(a). The pressure nodal plane (i.e., zero pressure amplitude) is formed at the center of the microchannel and a standing wave coordinate system $(x, y, z)$ is considered such that the $y$ axis is aligned with the pressure nodal plane. The entire device, without the presence of a microparticle, is simulated to obtain the acoustic pressure and streaming velocity fields. We assume the acoustic wave propagation to be isentropic and thus the pressure perturbations of the acoustic wave become proportional to the density perturbations only. In the bulk, where the fluid may be considered ideal in the frequency of MHz range, the assumption is well justified. Near the particles, the viscous and thermal stresses lead to the viscous and thermal boundary layer thickness. Considering the fluid as water at room temperature actuated at 2 MHz frequency, the thickness of viscous and thermal boundary layers are 0.4 and 0.2 $\mu$m, respectively [39]. Since we have considered the particle size of 8 $\mu$m, which is one order higher in size compared to the boundary layer thickness, thus we neglect the transient and thermoviscous effects in the present work, considering only the time-harmonic acoustic fields.
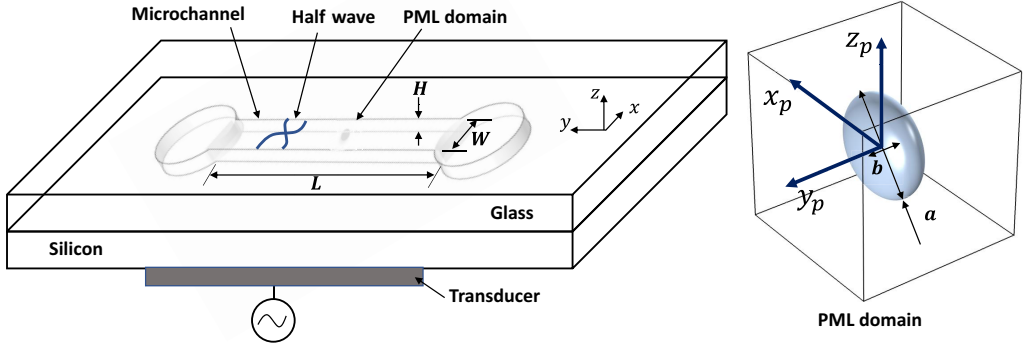
FIG. 1. Schematic of the acoustofluidics device used to calculate the acoustic pressure and streaming velocity fields. The device comprises a straight microchannel of width ($W$) 500 $\mu$m, height ($H$) 200 $\mu$m, and length ($L$) 3.5 mm. The channels are etched into the silicon substrate and a glass substrate is used for sealing the channel. Acoustic standing half wave is produced using a lead zirconate titanate (PZT) transducer. An oblate shaped particle having the length of the major axis ($a$) and minor axis ($b$) is placed in the microchannel and its translational and rotational dynamics are studied. Perfectly matched layer (PML) domain of size 20 $\mu$m × 20 $\mu$m × 20 $\mu$m with PML thickness 5 $\mu$m, having nonreflecting walls as the faces of a cube and encapsulating the particle is also shown. PML has the same property as fluid to avoid rescattering of the scattered wave into the computation domain.

Since the time-harmonic displacements of the different components are very small, we can model the solid domain using the first-order time-harmonic equations [40]. We assume that the loss due to the fluid element upon the solid domain is negligible. We consider the Fourier representation of the time domain as $A(\boldsymbol{r}, t) = A(\boldsymbol{r}, \omega)e^{-i\omega t}$, which is then used to formulate the relevant equations in the frequency domain. Here, $A$ is an arbitrary variable, $\boldsymbol{r}$ and $t$ denote the space and time, and $\omega$ is the angular frequency, related to the actuation frequency $f$ as $\omega = 2\pi f$. Now, we need to invoke the real part of the time-harmonic field, $\mathrm{Re}[A(r, \omega)e^{-i\omega t}]$ to obtain the physical values of the variables.

The solid components can be modeled using the Cauchy equation of motion in the frequency domain,

$$\nabla \cdot \boldsymbol{\sigma} + \rho\omega^2 \boldsymbol{v}_s = 0, \tag{11}$$

where $\boldsymbol{\sigma}$ is the stress acting on the material of density $\rho$ and $\boldsymbol{v}_s$ is the solid displacement field. Using the kinematic relation, we can relate the solid strain $\boldsymbol{\gamma}$ to that of the displacement field as

$$\boldsymbol{\gamma} = \tfrac{1}{2}[\nabla \boldsymbol{v}_s + (\nabla \boldsymbol{v}_s)^T]. \tag{12}$$

The stress and the displacement field for each solid component are related using the constitutive relation:

$$\boldsymbol{\sigma} = \boldsymbol{C} : \boldsymbol{\gamma}, \tag{13}$$

where $C$ is the isentropic elasticity tensor, which can be further divided into the storage and loss tensors as $C = C' + i\,C''$. Since the material damping for silicon is minute, the loss tensor can be neglected and only the storage tensor is considered in the present case [41]. Usually, the elasticity tensor is composed of 81 terms for an anisotropic material. However, for monocrystalline silicon for a (100) wafer, the combination of cubic symmetry and the equivalence of shear conditions reduces the fourth-order tensor to be represented by only three independent components [42]. Therefore, the

anisotropic material tensor can be written in Voigt notation as follows:

$$\boldsymbol{C} = \begin{bmatrix} C_{11} & C_{12} & C_{12} & 0 & 0 & 0 \\ C_{12} & C_{11} & C_{12} & 0 & 0 & 0 \\ C_{12} & C_{12} & C_{11} & 0 & 0 & 0 \\ 0 & 0 & 0 & C_{44} & 0 & 0 \\ 0 & 0 & 0 & 0 & C_{44} & 0 \\ 0 & 0 & 0 & 0 & 0 & C_{44} \end{bmatrix}. \tag{14}$$

We solve the above equations in COMSOL MULTIPHYSICS 5.4 to obtain the displacement fields by considering the materials to be linear elastic [24]. Linear elastic materials with anisotropic and isotropic models are used to simulate the silicon and glass substrates, respectively [22]. The terms of the elasticity matrix can be expressed in terms of Young's modulus $E$ and Poisson's ratio $\nu$ as

$$C_{11} = \frac{E(1 - \nu)}{(1 + \nu)(1 - 2\nu)}, \tag{15}$$

$$C_{12} = \frac{E\nu}{(1 + \nu)(1 - 2\nu)}. \tag{16}$$

For isotropic materials like glass, the elastic moduli are dependent, $C_{44} = (C_{11} - C_{12})/2$. The density and relative permittivity of the silicon substrate are taken to be 2330 kg/m$^3$ and 4.5, respectively, whereas for borosilicate glass, the values are taken to be 2230 kg/m$^3$ and 4.8, respectively. The Young's modulus and Poisson's ratio of borosilicate glass are taken as 63 GPa and 0.2, respectively. Further, the elasticity matrices are used to model the elastic behavior of the silicon and the values of the elasticity matrix coefficients, $C_{11}$, $C_{12}$, and $C_{44}$ for silicon are 166, 64, and 80 GPa, respectively. The density of the lead zirconate titanate (PZT) transducer is 7700 kg/m$^3$.

To solve for the displacement field of the transducer, an additional dependency of the stress field on the electric field is modeled using Gauss's law. Since the stress and charge are mutually dependent, the coupled relations can be written as

$$\nabla \cdot \boldsymbol{D} = 0, \tag{17}$$

$$\boldsymbol{\sigma}^S = \boldsymbol{C}^E : \boldsymbol{\gamma} + \boldsymbol{d}^T \cdot \nabla V, \tag{18}$$

$$\boldsymbol{D} = \boldsymbol{d} : \boldsymbol{\gamma} - \varepsilon_0 \boldsymbol{\varepsilon}_r^S \cdot \nabla V, \tag{19}$$

where $V$ is the electrostatic potential, $\boldsymbol{D}$ is the electric displacement field, $\mathbf{d}$ is the piezo coupling tensor, $\varepsilon_0$ represents the relative permittivity of the free space, and $\boldsymbol{\varepsilon}_r^s$ is the relative permittivity tensor under a constant strain.

For the PZT transducer, the elasticity, couplingand permittivity tensors are defined as

$$\boldsymbol{C}^E = \begin{bmatrix} C_{11}^E & C_{12}^E & C_{13}^E & 0 & 0 & 0 \\ C_{21}^E & C_{22}^E & C_{23}^E & 0 & 0 & 0 \\ C_{31}^E & C_{32}^E & C_{33}^E & 0 & 0 & 0 \\ 0 & 0 & 0 & C_{44}^E & 0 & 0 \\ 0 & 0 & 0 & 0 & C_{55}^E & 0 \\ 0 & 0 & 0 & 0 & 0 & C_{66}^E \end{bmatrix}, \tag{20}$$

$$\boldsymbol{d} = \begin{bmatrix} 0 & 0 & 0 & 0 & d_{15} & 0 \\ 0 & 0 & 0 & d_{15} & 0 & 0 \\ d_{31} & d_{31} & d_{33} & 0 & 0 & 0 \end{bmatrix}, \tag{21}$$

$$\boldsymbol{\varepsilon}_r^S = \begin{bmatrix} \varepsilon_{11}^S & 0 & 0 \\ 0 & \varepsilon_{22}^S & 0 \\ 0 & 0 & \varepsilon_{33}^S \end{bmatrix}. \tag{22}$$

The coefficients of the elasticity tensor are given by $C_{11}^E = C_{22}^E = 1.68 \times 10^{11}$ Pa, $C_{12}^E = C_{21}^E = 11.0 \times 10^{10}$ Pa, $C_{13}^E = C_{23}^E = C_{31}^E = C_{32}^E = 9.99 \times 10^{10}$ Pa, $C_{33}^E = 1.23 \times 10^{11}$ Pa, $C_{44}^E = C_{55}^E = 3.01 \times 10^{10}$ Pa, and $C_{66}^E = 2.88 \times 10^{10}$ Pa. The values of the coupling tensor coefficients are given by $d_{31} = 2.80$ C/m$^2$, $d_{33} = 14.69$ C/m$^2$, and $d_{15} = 9.86$ C/m$^2$. Finally, the values of the coefficients of the relative permittivity tensor are given by $\varepsilon_{11}^S = \varepsilon_2^S = 828$ and $\varepsilon_{33}^S = 700$ with the vacuum permittivity value as $\varepsilon_0 = 8.8542 \times 10^{12}$ C$^2$/m$^2$/N.

In the fluid domain, a purely time-harmonic model is not sufficient to understand the acoustic pressure field. One can obtain the first-order time-harmonic equations using the perturbation expansion technique. The Helmholtz equation is used to model the first-order acoustic pressure and velocity field as follows [19]:

$$\nabla^2 p_1 = -k^2 p_1, \tag{23}$$

where $p_1$ is the first-order time-harmonic pressure field, and $k$ is the complex wave number defined as $k = \frac{\omega}{c_1}$. Here, $c_1$ represents the complex speed of sound. The time-harmonic velocity field is obtained as

$$\boldsymbol{u}_1 = \frac{i}{\rho_0 \omega} \nabla p_1. \tag{24}$$

Material damping is implemented to enhance the time-harmonic amplitudes in a resonant state. The damping of the PZT device is modeled in terms of dielectric loss tangent and the mechanical quality factor [22]. Further, the glue layer between the transducer and the silicon layer is approximated as a thin elastic layer. The thickness of the glue layer is taken to be 0.2 $\mu$m with a Young's modulus of 5.576 GPa and Poisson's ratio of 0.3 [22]. The acoustics structure module is used to couple the solid domain to the pressure acoustics domain used to model the fluid region.

For simulating the streaming velocity field, we need to resolve the viscous boundary layer using an extremely fine computational mesh. However, it is computationally expensive to do this in the case of a three-dimensional system. We solve this issue by using the concept of limiting velocity [43]. Since the method requires a time-harmonic field outside the boundary layer, we can avoid the requirement for an extremely fine resolution of the mesh. The limiting velocity method is applicable only when there are no sharp edges in the computational domain. In the present study, since there are no sharp edges, we used the technique to model the acoustic streaming velocity field in the microchannel. Further, as we deal with a MHz frequency range, the viscous boundary layer thickness is negligible, which further justifies our approach. The limiting velocities, obtained from the analytical derivation of Nyborg [44] are given as [43]

$$u_L = -\frac{1}{4\omega}\mathrm{Re}\left\{ u_1 \frac{du_1^*}{dx} + v_1 \frac{du_1^*}{dy} + u_1^*\left[ (2+i)\left( \frac{du_1}{dx} + \frac{dv_1}{dy} + \frac{dw_1}{dz} \right) - (2+3i)\frac{dw_1}{dz} \right] \right\}, \tag{25}$$

$$v_L = -\frac{1}{4\omega}\mathrm{Re}\left\{ u_1 \frac{dv_1^*}{dx} + v_1 \frac{dv_1^*}{dy} + v_1^*\left[ (2+i)\left( \frac{du_1}{dx} + \frac{dv_1}{dy} + \frac{dw_1}{dz} \right) - (2+3i)\frac{dw_1}{dz} \right] \right\}, \tag{26}$$

where the asterisk denotes complex conjugation; $u_L$ and $v_L$ represent the two components of the limiting velocities over a vibrating surface; $u_1$, $v_1$, and $w_1$ are the three components of first-order acoustic velocities along coordinates $x$, $y$, and $z$.

The governing equations for the second-order pressure and streaming velocity field are given by [45]

$$\nabla p_2 = \eta \nabla^2 \boldsymbol{u}_2, \tag{27}$$

$$\nabla \cdot \boldsymbol{u}_2 = 0. \tag{28}$$

The two equations above are solved to obtain the acoustic pressure and velocity fields, as discussed in the next section.

### D. Numerical simulation of the particle dynamics

The pressure and acoustic streaming velocity fields obtained from the device model are used as the background acoustic field to calculate the acoustic scattering field for a nonspherical particle. Since we have considered only a single particle inside the domain, we consider the incoming acoustic field to calculate the acoustic radiation force and torque acting on the particle.

In acoustofluidics, the dynamics of a particle are mainly governed by acoustic radiation force, buoyancy force, and streaming-induced drag force. Further, we assume that the particle trajectory does not change due to the inertial effects. For a nonspherical particle, the governing equation that describes the 3D motion of the particle is given by [22]

$$\begin{bmatrix} \boldsymbol{F_r} \\ \boldsymbol{T_r} \end{bmatrix} + \begin{bmatrix} \boldsymbol{F_b} \\ 0 \end{bmatrix} = \boldsymbol{L}\left( \begin{bmatrix} \boldsymbol{u} \\ \boldsymbol{\omega} \end{bmatrix} - \begin{bmatrix} \boldsymbol{u^s} \\ \boldsymbol{\omega^s} \end{bmatrix} \right), \tag{29}$$

where $\boldsymbol{F_r}$ and $\boldsymbol{T_r}$ are the acoustic radiation force and torque given by Eqs. (7) and (8), respectively, $\boldsymbol{F_b}$ denotes the buoyancy force, and $\boldsymbol{L}$ is the hydrodynamic resistance matrix. The particle translational and rotational velocity are given by $\boldsymbol{u}$ and $\boldsymbol{\omega}$, respectively, and the terms $\boldsymbol{u^s}$ and $\boldsymbol{\omega^s}$ are the streaming velocity and streaming vorticity, respectively.

The hydrodynamics resistance matrix $\boldsymbol{L}$ can be written as a block matrix:

$$\boldsymbol{L} = \begin{pmatrix} \boldsymbol{K} & \boldsymbol{C_s^T} \\ \boldsymbol{C_s} & \boldsymbol{\Omega_s} \end{pmatrix}. \tag{30}$$

The submatrices $\boldsymbol{K}$, $\boldsymbol{C_s}$, and $\boldsymbol{\Omega_s}$ are $3 \times 3$ dimensional submatrices that represent the translational tensor, translational-rotational coupling tensor, and rotational tensor, respectively. Here, the translational and rotational tensors are symmetric, while the translational-rotational coupling tensor is nonsymmetric. In the present case, the symmetricity of the particle leads to a diagonal hydrodynamic matrix where all the nondiagonal terms are zero. We obtained the coefficients of the $\boldsymbol{L}$ matrix numerically using a creeping flow simulation around the particle. By taking the particle translational and rotational motion in the three coordinate directions, we obtained each column of the $\boldsymbol{L}$ matrix. For example, the first column can be obtained by considering the translational motion along the $x$ direction as

$$\begin{bmatrix} L_{11} \\ \vdots \\ L_{61} \end{bmatrix} = -\frac{1}{v_{px}} \begin{bmatrix} \boldsymbol{F_r} \\ \boldsymbol{T_r} \end{bmatrix}. \tag{31}$$

Here, $v_{px}$ is the prescribed translational velocity of the particle in the $x$ direction. The calculation procedure for other columns of the hydrodynamics resistance matrix is discussed in Sec. S1 of the Supplemental Material [46].

We have chosen the fluid region as a large cylindrical domain with an oblate shaped particle placed at its center. A large fluid domain is considered to minimize the particle-wall interactions, which otherwise may affect the hydrodynamics resistance coefficients [22]. The hydrodynamic resistance matrix contains the drag coefficient matrix, translational-rotational coupling, and the rotational matrix, and therefore the size of the matrix is $6 \times 6$ with 36 parameters. For an oblate shaped particle, we obtained these parameters using the creeping flow simulations around the particle by solving the Stokes equations without the body force term as follows,

$$\eta \nabla^2 \boldsymbol{v_c} = \nabla p_c, \tag{32}$$

$$\nabla \cdot \boldsymbol{v_c} = 0, \tag{33}$$

where $v_c$ and $p_c$ represent the creeping flow velocity and pressure, respectively, and $\eta$ is the dynamic viscosity of the fluid. Here, we have used the creeping flow module in COMSOL, similar to that done in [22] as the surrounding fluid is stationary. We also performed simulations using the laminar flow module which yielded identical results. However, in the case of a moving fluid system one needs
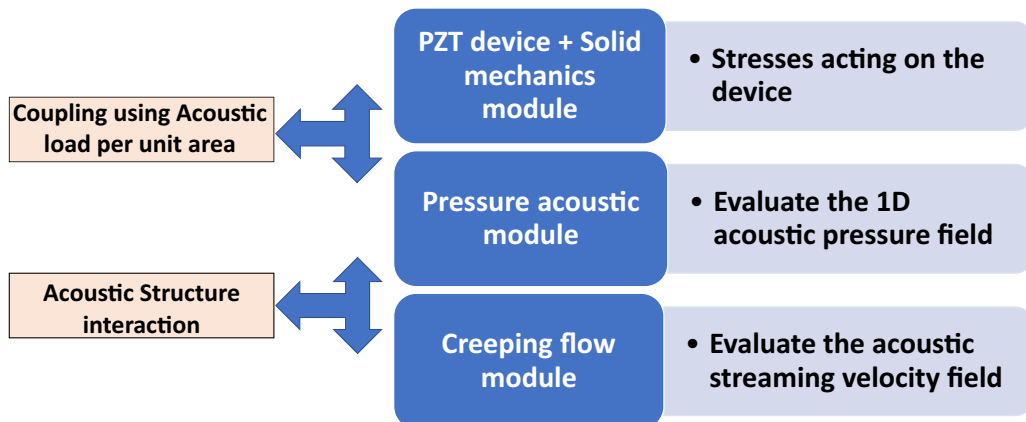
FIG. 2. The structure of the numerical setup including the coupling between the different modules that constitute a full device model.

to use the laminar flow module instead of the creeing flow module. To determine each column of the 6×6 matrix, six linearly independent motions are prescribed, viz., translational and rotational motion along the three Cartesian axes. Further, due to the symmetricity of the object, only the diagonal terms remain, and all other terms of the matrix are equal to zero. The simulation results for the creeping flow velocity and pressure are presented in the next section.

### III. RESULTS AND DISCUSSIONS

In this section, first, we present and discuss the device simulation results on the pressure and velocity fields. Then, we validate our numerical model by comparing the acoustic radiation force computed using our model with that from an existing analytical model. Further, the effects of initial orientation, aspect ratio, particle size, and initial position on the translational and rotational behavior of an oblate shaped particle are presented and discussed.

#### A. Device simulation—acoustic pressure and streaming velocity fields

We simulated the acoustofluidics device comprising a lead zirconate titanate (PZT) transducer, a glue layer, a silicon layer, and a borosilicate glass layer to obtain the pressure and velocity fields inside the microchannel. The density and speed of sound of the fluid are taken as $\rho = 997 \, \text{kg/m}^3$ and $c = 1497 \, \text{m/s}$, respectively. The structure of the numerical setup including the coupling between the different modules that constitute a full device model is shown in Fig. 2. A potential difference of 2.5 V is established across the transducer using the piezoelectric module. The piezoelectric effects are coupled with the solid mechanics module to obtain the displacement and electric potential across the microchannel. The glue layer between the transducer and silicon layer is modeled as a thin elastic layer [40]. For the given dimensions of the microchannel of width $W = 500 \, \mu\text{m}$, height $H = 200 \, \mu\text{m}$, and length $L = 3.5 \, \text{mm}$, and a transducer attached to the silicon layer, a half wavelength is created at a resonating frequency of 1.44 MHz. It is to be noted that the pressure difference across the channel is kept to zero so there is no pressure-driven flow inside the microchannel, and flow occurs only due to the acoustic streaming effects. We obtained the acoustic pressure field in the fluid domain inside the microchannel, and its effect is coupled with that of the solid using a boundary load condition. Finally, the second-order velocity field is obtained by solving the creeping flow equations, i.e., Eqs. (30) and (31). The acoustic pressure field shows that the nodal plane is present at the center of the microchannel in the width direction, as shown in Fig. 3(a). The acoustic streaming velocity field is as shown in Fig. 3(b), and a zoomed-in view of
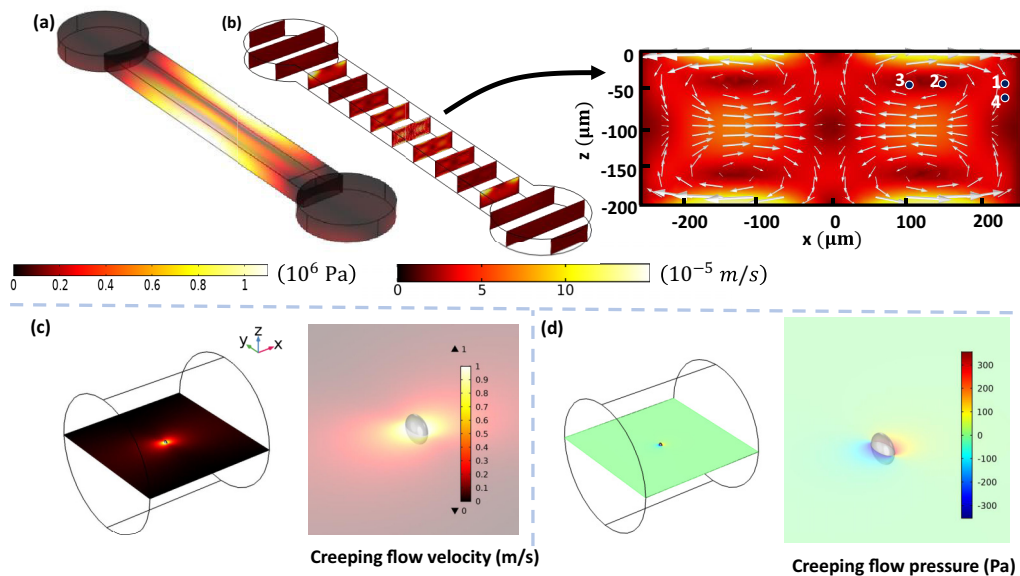
FIG. 3. (a) First-order acoustic pressure field inside the microchannel, frequency 1.44 MHz, wavelength 1000 $\mu$m along the width of the channel; pressure node is created at the middle of the channel in the width direction (*x* direction) (0 MPa, gray; 1.17 MPa, creamy white). (b) Acoustic streaming field is generated inside the microchannel using the limiting velocity boundary condition. A zoomed-in view of the acoustic streaming field in the *x*-*z* plane at $y = 0$ $\mu$m, i.e., midpoint of the microchannel along its length, is also shown. The clockwise and counterclockwise streaming field is observed in the *x*-*z* plane. Simulation results for the (c) creeping flow velocity, and (d) creeping flow pressure contours.

the microchannel cross section shows the formation of four recirculation vortices, two vortices in the clockwise direction and two vortices in the anticlockwise direction.

The obtained fluid velocity and pressure field around the oblate shaped particle using the creeping flow simulations are shown in Figs. 3(c) and 3(d), respectively. Identical fluid velocity and pressure fields, and the same value of drag coefficient are obtained using the laminar flow module in COMSOL and the results are presented in Fig. S1 in the Supplemental Material [46]. A large cylindrical domain is taken for the flow simulation to avoid any effects of the particle-wall interactions on the fluid dynamics. The fluid velocity is observed to be maximum at the particle surface and decays continuously as we move away from the particle. For a prescribed particle surface velocity of 1 m/s, the fluid pressure field is shown in Fig. 3(d). The maximum absolute value of the pressure field is obtained about 300 Pa near the particle interface, and similar to velocity, the pressure decays to zero at the cylinder wall. The forces and torques are obtained from the surface traction on the particle surface, while the desired rotation and translational motion are evaluated by prescribing the velocity to the particle in the three Cartesian directions. We have calculated the values of the diagonal terms for different sizes and aspect ratios of particles and present the values in Table I. It is to be noted that, due to symmetry, the *y*- and *z*-translational components $L_{22}$ and $L_{33}$ are equal. Similarly, the rotational components about the *y* and *z* axes represented by $L_{55}$ and $L_{66}$ are also the same.

## B. Model validation

Before we proceed to study the dynamical behavior of an oblate shaped particle, the proposed numerical model is validated by comparing the acoustic radiation force acting on the particle predicted from the model with that obtained from an existing analytical expression [12]. The particle density and speed of sound are taken as 1136 kg/m$^3$ and 1680 m/s, respectively. The compressibility of the particle is $1.91 \times 10^6$ kg/m$^2$ s. The elasticity and Poisson's ratio of the

TABLE I. Values of the hydrodynamic resistance matrix coefficients for various particle sizes and aspect ratios.

| Dimension | $L_{11}$ (N s m$^{-1}$) | $L_{22}$ (N s m$^{-1}$) | $L_{33}$ (N s m$^{-1}$) | $L_{44}$ (N m s) | $L_{55}$ (N m s) | $L_{66}$ (N m s) |
|---|---|---|---|---|---|---|
| $a = 8 \ \mu$m$(a/b) = 2$ | $5.98 \times 10^{-8}$ | $5.39 \times 10^{-8}$ | $5.39 \times 10^{-8}$ | $9.72 \times 10^{-19}$ | $7.77 \times 10^{-19}$ | $7.77 \times 10^{-19}$ |
| $a = 12 \ \mu$m$(a/b) = 2$ | $9.11 \times 10^{-8}$ | $8.28 \times 10^{-8}$ | $8.28 \times 10^{-8}$ | $3.32 \times 10^{-18}$ | $2.66 \times 10^{-18}$ | $2.66 \times 10^{-18}$ |
| $a = 16 \ \mu$m$(a/b) = 2$ | $1.22 \times 10^{-7}$ | $1.12 \times 10^{-7}$ | $1.12 \times 10^{-7}$ | $7.89 \times 10^{-18}$ | $6.34 \times 10^{-18}$ | $6.34 \times 10^{-18}$ |
| $a = 9.12 \ \mu$m$(a/b) = 3$ | $6.52 \times 10^{-8}$ | $5.55 \times 10^{-8}$ | $5.55 \times 10^{-8}$ | $1.23 \times 10^{-18}$ | $9.74 \times 10^{-19}$ | $9.74 \times 10^{-19}$ |
| $a = 10.08 \ \mu$m$(a/b) = 4$ | $6.95 \times 10^{-8}$ | $5.76 \times 10^{-8}$ | $5.76 \times 10^{-8}$ | $1.5 \times 10^{-18}$ | $1.19 \times 10^{-18}$ | $1.19 \times 10^{-18}$ |
| $a = 10.85 \ \mu$m$(a/b) = 5$ | $7.31 \times 10^{-8}$ | $5.95 \times 10^{-8}$ | $5.95 \times 10^{-8}$ | $1.75 \times 10^{-18}$ | $1.41 \times 10^{-18}$ | $1.41 \times 10^{-18}$ |

particle are taken as 2.7311 GPa and 0.35, respectively. The acoustic radiation force acting on a spheroid shaped particle exposed to a bulk acoustic standing wave is analytically approximated using the acoustic radiation force function, $Y_{st}$ as follows [12],

$$\mathbf{F_r} = E_{ac}\pi R^2 Y_{st}\sin(2kx)\mathbf{e_x}, \tag{34}$$

where $E_{ac}$ denotes the acoustic energy density, and $R$ is the radius of the particle in the spherical limit. The radiation force acting on the spheroid particle can be expressed in terms of the spherical particle of the same volume given by King's expression, given as [12,47,48]

$$\mathbf{F_r} = \left(1 + \tfrac{6}{25}\epsilon_s + \tfrac{9}{875}\epsilon_s^2 + \cdots\right)\mathbf{F_r^{King}} \tag{35}$$

where spheroid eccentricity is defined as $\epsilon_s = (a/b) - 1$.

The acoustic radiation force acting on a rigid sphere predicted by King is given as $\mathbf{F_r^{King}} = 4\pi R^3 E_{ac}k\phi \sin(2kx)\mathbf{e_x}$, where the contrast factor $\phi = \frac{1 + (\frac{2}{3})(1 - \rho_f/\rho_p)}{2 + \rho_f/\rho_p}$ and $E_{ac}$ is the acoustic energy density defined in terms of incoming acoustic pressure amplitude as $E_{ac} = \frac{p_a^2}{4\rho c^2}$ [2,8]. The acoustic force function using the King's formula is given by

$$Y_{st} = 4(kR)\phi. \tag{36}$$

For a fixed rigid sphere, the ratio of the density of fluid to density of particle is $\frac{\rho_f}{\rho_p} = 0$. The contrast factor is equal to $\phi = 5/6$ and the corresponding acoustic force function $Y_{st} = \frac{10}{3}(kR)$. If the definition of the acoustic energy density is considered as $E_{ac} = \frac{p_a^2}{8\rho c^2}$ as defined in Ref. [49], the acoustic force function for the fixed rigid sphere is given by

$$Y_{st} = 8(kR)\phi = \frac{20}{3}(kR). \tag{37}$$

This shows that in the limit of the rigid fixed sphere ($\frac{\rho_f}{\rho_p} = 0$), the Marston [50] expression for a spherical particle and King's theory [8] agree with each other. However, for a particle with finite density the corresponding acoustic force function will deviate from that given by Eq. (37). Let us consider a numerical example taken by Hasegawa in his paper: a rigid sphere with $\frac{\rho_p}{\rho_f} = 10$ and $kR = 0.1$; the value of $Y_{st}$ from Ref. [49] is 0.612. The contrast factor is equal to $\phi = 0.7619$. Using the formulation of King, the $Y_{st}$ is given by 0.608 for the same particle. The value of $Y_{st}$ obtained from the present simulation for the same density ratio and $kR = 0.1$ is $Y_{st} = 0.603$, which is in good agreement with the results of King and Hasegawa. In the present case, the density ratio $\frac{\rho_f}{\rho_p} = 0.877$; using Eq. (36) the acoustic force function value for $kR = 0.1$ is given by $Y_{st} = 0.150$. The value of the acoustic force function obtained from the simulation model for the same density ratio is given by $Y_{st} = 0.147$ which agrees with the obtained value from te King's expression.

We have used both Marston's and King's analytical expressions for an oblate and a spherical shape particle, respectively, to validate our model. The variation of the acoustic radiation force
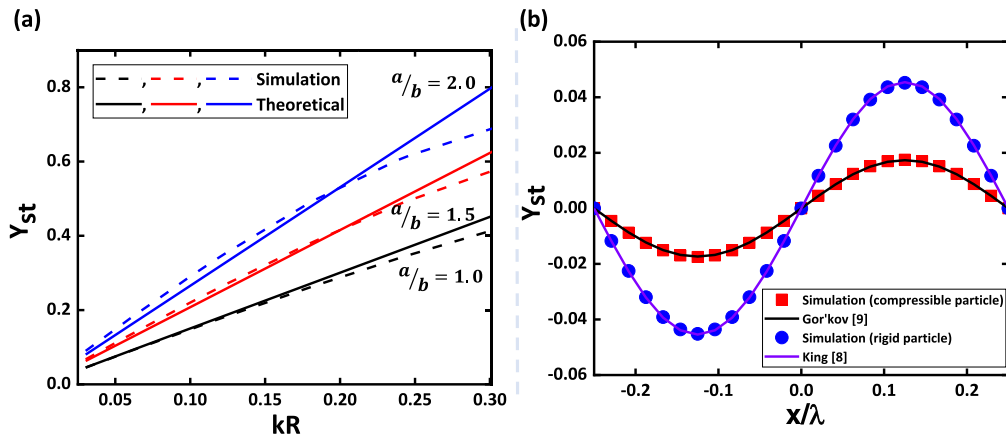
FIG. 4. (a) The variation of acoustic radiation force function ($Y_{st}$) for a rigid particle with finite mass with the normalized particle radius ($kR$) obtained from our numerical model and calculated from the existing analytical expression [Eq. (35)]. The numerical results are shown by the dotted lines, and the analytical predictions are indicated by the solid lines. (b) Variation of acoustic radiation force function ($Y_{st}$) with the normalized particle position ($x/\lambda$) obtained from simulations and existing analytical models for a rigid and compressible spherical particle of radius $kR = 0.0483$.

function with the normalized particle radius ($kR$) for three different aspect ratios, viz., $a/b = 1$, 1.5, and 2, is shown in Fig. 4(a). In this case, the particle is positioned at $x = \lambda/8$, where $\lambda$ is the wavelength of the acoustic wave, as it experiences the maximum acoustic force at this location. An excellent match between our simulation results and the predictions from King's analytical model is observed for an aspect ratio of 1.0 for a particle radius $kR < 0.2$. A small difference between the simulation results and the theoretical predictions is observed for larger particle size, $kR \geqslant 0.2$, due to the Rayleigh limit assumptions (i.e., $\lambda \gg R$) used in deriving the analytical solution for a spherical particle [8]. For aspect ratio, $(a/b) = 1.5$ and 2, there is a good match between the simulations and analytical results given by Eq. (35) for normalized particle size, $kR < 0.2$.

Further, simulations are carried out considering a spherical particle of radius 8 $\mu$m ($kR = 0.0483$) to be rigid and compressible, separately. The variation of acoustic force function ($Y_{st}$) with the particle position for compressible and rigid spherical particles is presented in Fig. 4(b). The simulation results are compared with the existing analytical results of Gor'kov and King for a spherical and rigid particle, respectively. Our simulation results match with analytical results for a rigid and a compressible particle in the range $kR \ll 0.1$.

## C. Dynamical motion of an oblate shaped particle

We studied the dynamical motion of an oblate shaped microparticle of size $a = 8$ $\mu$m and $b = 4$ $\mu$m, as the lengths of the major and minor axis, respectively, when exposed to a bulk acoustic wave inside a microchannel. As discussed earlier, the acoustic pressure and streaming velocity fields are obtained from the device model, and using the pressure and velocity fields as the background acoustic field, we simulated the transient behavior of the oblate shaped particle. To start with, we explore the effects of the initial orientation of the particle (i.e., the alignment of the particle with the pressure nodal plane).

### 1. Effects of the initial orientation of the particle

To understand the effect of the initial particle orientation on its rotational and translational motion, the initial orientation of the particle is varied with reference to the acoustic wave direction,
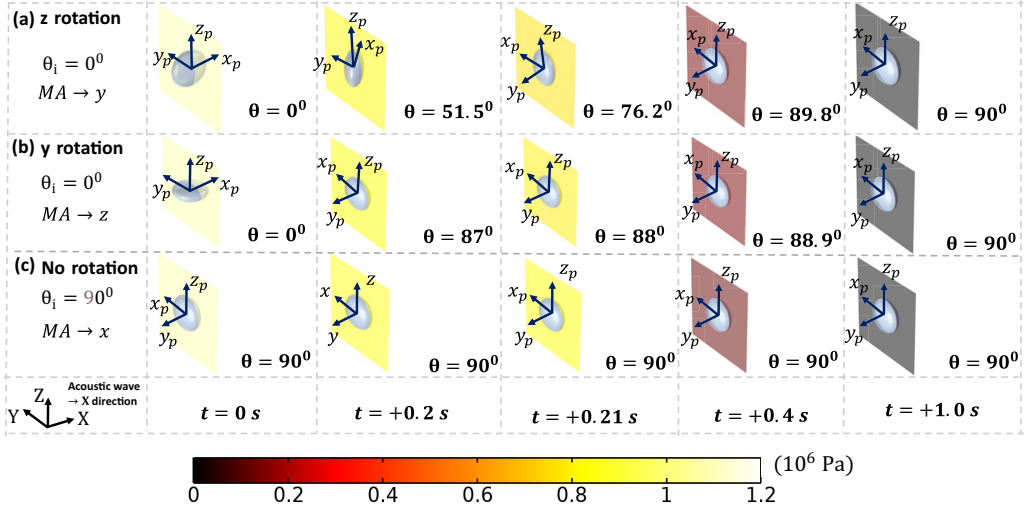
FIG. 5. The time-lapse images showing the rotational dynamics of an oblate shaped particle exposed to a bulk acoustic standing wave along the $x$ direction. (a) Rotation of the particle is observed about the $z$ axis when the particle minor axis (MA) is initially along the $y$ direction; i.e., particle coordinates are aligned with the standing wave coordinate axes, $\theta_i = 0°$. (b) Rotation of the particle is observed about the $y$ axis when the particle MA is initially along the $z$ direction; i.e., $(x_p, y_p, z_p)$ are aligned with the $(x, y, z)$ coordinate system, $\theta_i = 0°$. (c) Rotation is not observed when the particle MA is initially aligned in the standing wave direction; i.e., particle coordinates are perpendicular to the standing wave coordinates system, $\theta_i = 90°$. The amplitude of the acoustic pressure is spatially varying from 1.2 MPa near the wall (pressure antinode) to 0 MPa at the center (pressure node) of the microchannel. The color contours in the planes represent the magnitude of the acoustic pressure at various locations inside the microchannel. (See Supplemental Videos S1–S3, corresponding to $z$ rotation, $y$ rotation, and no rotation cases, respectively [46]).

i.e., $x$ direction. The orientation angle $\theta$ is defined as the angle between the major axis of the particle and the standing wave direction. The coordinate system is shown in Fig. 1 with its origin $(0, 0, 0)$ at the geometric center of the microchannel, and the particle is initially placed at the location $x = 240\ \mu\mathrm{m}, y = 0\ \mu\mathrm{m},$ and $z = -50\ \mu\mathrm{m}$, away from the pressure nodal plane, which allows us to study its translational and rotational behavior when exposed to a bulk acoustic wave. The particle with major and minor axes $a$ and $b$ is placed inside a perfectly matched layer (PML) domain as depicted in Fig. 1. A particle coordinate system with the origin attached to the center of the particle is considered [see Fig. 1(b)]. When the minor axis (MA) is along the $y_p$ or $z_p$ direction, then the particle coordinate system and standing wave coordinate system are aligned to each other which implies that the initial orientation angle $\theta_i = 0°$. The major axis of the particle which is along the $x_p$ direction is aligned with the $x$ direction of the standing wave coordinate. The time-lapse images showing the rotational dynamics of the particle in such a case are shown in Fig. 5(a). We observe that the particle continues to rotate about the $z$ axis until the principal axis is perpendicular to the wave direction while translating toward the pressure nodal plane. This suggests that finally the minor axis is aligned with the pressure wave direction, resulting in a final orientation angle, $\theta_f = 90°$. Similarly, when the particle is initially placed with its MA is along the $z_p$ axis, the particle continues to rotate about the $y$ axis, as shown in Fig. 5(b). Since there are two major axes and one minor axis for an oblate shaped particle, we observe both $y$ and $z$ rotation of the particle. In the case when the MA is aligned along the $x$ direction, the particle coordinate system and standing wave coordinate system are perpendicular to each other and orientation angle $\theta_i$ becomes $90°$. Rotation of the particle is not observed in such a case, as shown in Fig. 5(c). The rotation and migration dynamics of
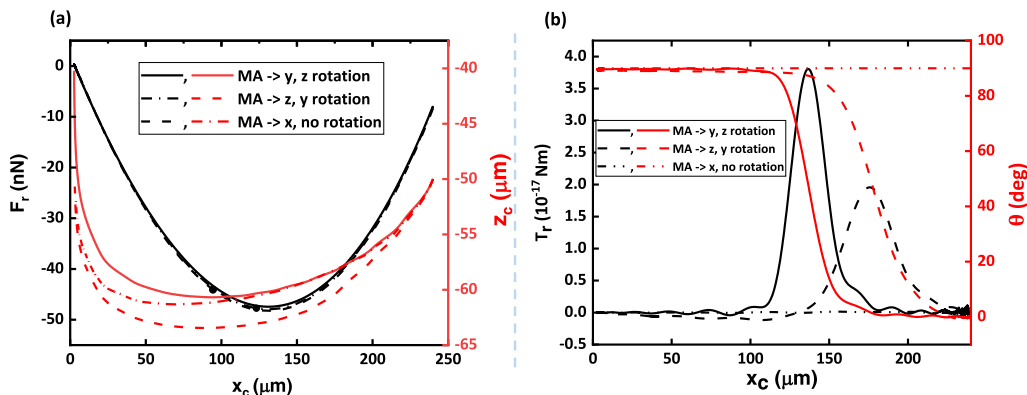
FIG. 6. (a) The $x$-$z$ trajectories of the particles with different initial orientations, i.e., the minor axis (MA) along the $x$, $y$, or $z$ direction; the variation in the acoustic radiation force with the $x$ coordinate of the center of the particle is also presented. (b) The variation of the orientation angle and acoustic radiation torque acting on the particle with different initial orientations with the position of the center of the particle along the $x$ direction. In all cases, $V = 1.34 \times 10^{-16}$ m$^3$, $(a/b) = 2$, and the initial location of the particle center $x_{ci} = 240$ $\mu$m and $z_{ci} = -50$ $\mu$m.

an oblate shaped particle at different initial orientations, with its minor axis at a 45° angle with the $y$ and $z$ directions (i.e., $\theta_i = 135°$), are shown in Fig. S2 in the Supplemental Material [46]. The variation of particle trajectory, angle, angular velocity, acoustic radiation force, and acoustic radiation torque with the particle center along the $x$ axis are plotted in Fig. S3 [46]. Therefore, we find that whenever the minor axis of the particle is not aligned with the pressure wave direction, i.e., $\theta_i \neq 90°$, rotation of the particle is observed, which suggests that the particle is in an orientation that corresponds to an unstable equilibrium state whenever $\theta_i \neq 90°$. Upon exposure to the acoustic field, the particle rotates in order to achieve an orientation that corresponds to a stable equilibrium state. In the time-lapse images, the change in the color of the $x$-$y$ planes cutting through the particle shows a decrease in the magnitude of acoustic pressure indicating that the particle translates toward the pressure nodal plane, i.e., along the $x$ direction.

The $x$-$z$ trajectories of particles with different initial orientations presented above along with the variation in the acoustic radiation force acting on it as a function of the position of the particle center in the $x$ direction are presented in Fig. 6(a). The trajectories reveal that the particles move along a curved path in the $x$-$z$ plane—there is a motion in the $z$ direction while translating toward the pressure node along the $x$ direction. The movement of particles along the $z$ direction can be attributed to the streaming velocity field, which constitutes the circulation vortices in the $x$-$z$ plane, perpendicular to the wave direction [see Fig. 3(b)]. The particles follow the streaming velocity field while translating toward the pressure node. For the three different initial orientations presented above, the profiles showing the variation of the acoustic radiation force overlap as the radiation force acting on the particle is independent of the particle orientation. As the radiation force acting on the particles in the three different cases is the same, the particle velocities resulting from the radiation force acting on the particle are the same and hence the particle translation characteristics are identical. However, as the rotational behaviors are different, depending on the rotation angle the streaming-induced drag force will be different and hence the trajectories do not overlap.

The variation of the orientation angle and acoustic radiation torque acting on the particle with the position of the center of the particles along the $x$ direction is presented in Fig. 6(b). We see that the particle starts rotating only when the minor axis is not aligned with the pressure wave direction, the $x$ direction, i.e., when the particle is in an unstable orientation state. When the minor axis is positioned along the $y$ axis, i.e., along the microchannel, the particle translates some distance, until $x_c = 180$ $\mu$m, as shown in Fig. 6(b), toward the pressure node first before rotating about the
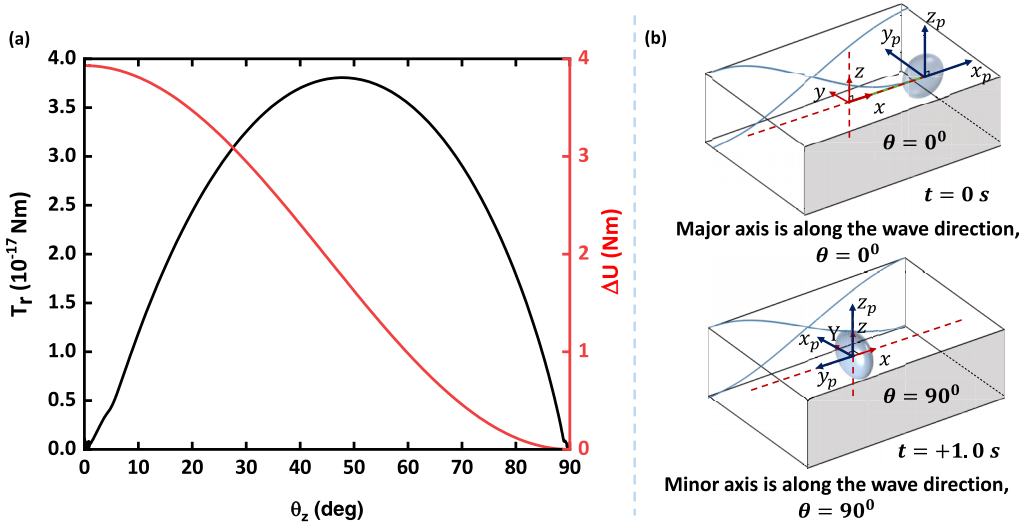
FIG. 7. (a) The variation of acoustic radiation torque and torque potential acting on the particle with the rotation angle; acoustic radiation torque is obtained from our simulations and torque potential is obtained from the analytical expression [25]. (b) Upper: initial location of the particle away from the pressure node; the particle is aligned such that the major axis is along the pressure wave direction, i.e., $x$ axis, with $\theta = 0°$. (ii) Final location of the particle at the pressure nodal plane; the minor axis of the particle is aligned with the pressure wave direction, i.e., $x$ axis, with $\theta = 90°$.

$z$ direction. Initial nonrotation of the particle can be attributed to the fact that torque acting on the particle is zero initially until the particle translates to $x_c = 180 \ \mu$m. Further, the acoustic radiation torque increases and reaches a maximum at $x \approx 138 \ \mu$m and then decreases further and finally approaches zero. It is observed that the particle rotation occurs at the point of maximum torque, i.e., $x \approx 138 \ \mu$m, as shown in Fig. 6(b). A similar trend is observed when the minor axis is positioned along the $z$ direction, i.e., along the pressure wave direction. The particle rotates about the $y$ axis to align its minor axis along the pressure wave direction, with the maximum torque occurring at $x \approx 164 \ \mu$m, relatively far away from the pressure node compared to the $z$-rotation case. The variation of angular velocity with the particle position is presented in Fig. S4(a) in the Supplemental Material [46]. As the torque value is nonzero from the original starting position of the particle, the particle rotates much faster in the $y$-rotation case, within 0.3 s compared to the $z$-rotation case, which takes about 0.5 s. Further, the magnitude of the maximum torque acting on the particle in the case of $y$ rotation is approximately half compared to the $z$-rotation case as shown in Fig. 6(b). Further, when the minor axis of the particle is aligned with the pressure wave direction, we observe the particle does not rotate, suggesting that the particle is already in a stable orientation state.

The rotational behavior of particles with different initial orientations presented above can be explained in terms of the acoustic torque potential, $\Delta U = \frac{\tau_0}{2} \cos(\theta)^2$, as shown in Fig. 7(a), where $\theta$ is the angle at which the major axis is inclined with the pressure wave direction, and $\tau_0$ is the characteristic torque [25]. From this expression, we see that if the major axis in the $x_p$ direction is aligned with the $x$ coordinate of the standing wave, i.e., $\theta = 0°$, the particle experiences the maximum torque potential. Therefore, the particle is in an unstable equilibrium orientation, although the acoustic radiation torque obtained from our simulation is initially zero. The particle tends to minimize the torque potential by undergoing rotation and aligning its minor axis along the wave direction to attain the stable orientation state, as shown in Fig. 7(b), wherein both the torque and torque potential vanish. The value of the torque is initially zero when $\theta = 0°$, attains a maximum at an orientation angle $\theta = 45°$, and gradually decreases to zero again when the minor axis of the
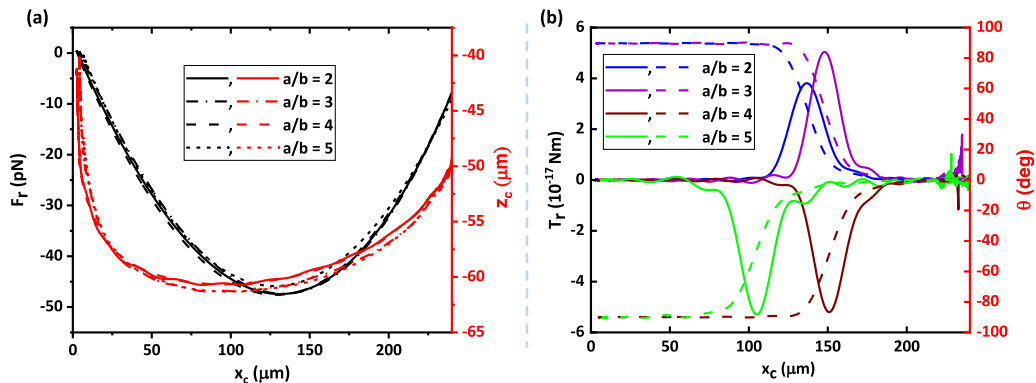
FIG. 8. (a) The $x$-$z$ trajectories of the particles and the variation in the acoustic radiation force along the $x$ coordinate of the center of the particles, for different aspect ratios. (b) The variation of the orientation angle (shown by dashed lines) and acoustic radiation torque (indicated by the solid lines) acting on the particles with the position of the center of the particles along the $x$ direction for different aspect ratios. Initial orientation: MA along the $y$ direction and $\theta_i = 0°$, particle volume fixed ($V = 1.34 \times 10^{-16}$ m$^3$).

particle is oriented along the pressure wave direction, i.e., $\theta = 90°$. As the particle rotates about the $z$ axis, the particle's coordinate system ($x_p, y_p, z_p$) becomes perpendicular to the standing wave coordinate system ($x, y, z$) as shown in Fig. 7(b). The above analytical results [25] are in agreement with our simulation results shown in Fig. 6(b), the value of the torque is maximum at $\theta = 45°$, at which the slope of the $\theta$ versus $x_c$ curve is the maximum, indicating a much faster rotation. Therefore, when the minor axis $y_p$ of the particle is initially along the pressure wave direction, i.e., $\theta = 90$ degree, the torque potential is zero which corresponds to a stable orientation state and rotational motion of the particle is not observed.

### 2. Effects of aspect ratio and volume of the particle

We examine the dynamical behavior of an oblate shaped particle by varying its aspect ratio, i.e., the ratio of the major to the minor axis ($a/b$), and volume ($V$). First, keeping the volume fixed ($V = 1.34 \times 10^{-16}$ m$^3$), we varied the aspects ratio as ($a/b$) = 2−5, and observed its effect on the dynamical motion of the particle. The particle is initially placed at $x_{ci} = 240$ $\mu$m, $y_{ci} = 0$ $\mu$m, and $z_{ci} = −50$ $\mu$m with its minor axis positioned along the axis of the microchannel, i.e., $\theta = 0°$. We observe that the acoustic radiation force acting on the particle has the same magnitude irrespective of the aspect ratio, as shown in Fig. 8(a). From theory [2], the radiation force is directly proportional to the particle volume, contrast factor, and its location inside the microchannel. As the particle volume remains fixed, merely changing the aspect ratio of the particle does not alter the magnitude of the acoustic radiation force. Consequently, the particle trajectories toward the pressure node in the $x$-$z$ plane for the different aspect ratios overlap, as shown in Fig. 8(a). The variation of the orientation angle and acoustic radiation torque acting on the particle with the position of the center of the particles along the $x$ direction is presented in Fig. 8(b). We find that the radiation torque acting on the particle changes its direction after a critical aspect ratio, ($a/b$) = 3. When viewed along the positive $z$ axis, the particle rotates in the anticlockwise direction for ($a/b$) = 2 and 3 and the clockwise direction for an aspect ratio of ($a/b$) = 4 and 5. We see that the direction of the torque changes its sign at the critical aspect ratio, ($a/b$) = 3, which explains why the direction of rotation of the particle is flipped.

The change in the sign of the torque is attributed to the displacement vector **r** in Eq. (8), which is defined as the distance between the center of mass and a point on the surface of the particle. The components of the radiation torque about the $z$ axis can be written as $\tau_z = (x - x_c) \times [\{-\frac{\rho_0}{2}\langle|v_1|^2\rangle + \frac{\rho_0}{2c_0^2}\langle(\partial_t\phi_1)\rangle^2\}n_y + \rho_0(\mathbf{n} \cdot \langle\mathbf{v}_1\rangle)\langle\mathbf{v}_1 \cdot \mathbf{n_y}\rangle] -$
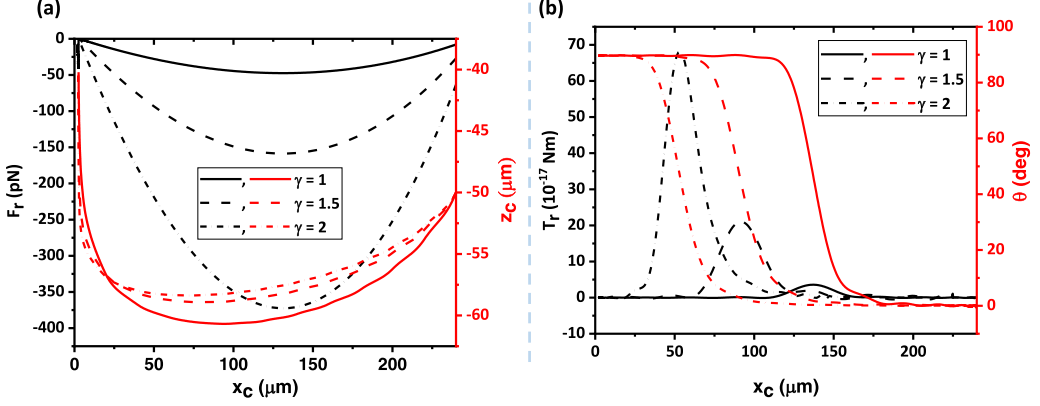
FIG. 9. (a) The $x$-$z$ trajectories of the particles and the variation in the acoustic radiation force along the $x$ coordinate of the center of the particles, for different particle volume ratios. (b) The variation of the orientation angle and acoustic radiation torque acting on the particles with the position of the center of the particles along the $x$ direction for different particle volume ratios. Initial orientation: MA along the $y$ direction and $\theta_i = 0°$, particle aspect ratio fixed $(a/b) = 2$, initial location, $x_{ci} = 240$ $\mu$m, $z_{ci} = -50$ $\mu$m.

$(y - y_c) \times [\{-\frac{\rho_0}{2}\langle|v_1|^2\rangle + \frac{\rho_0}{2c_0^2}\langle(\partial_t\phi_1)\rangle^2\}n_x + \rho_0(\mathbf{n} \cdot \langle\mathbf{v}_1\rangle)\langle\mathbf{v}_1 \cdot \mathbf{n_x}\rangle]$. Here, $x$ and $y$ are the coordinates of the points on the particle surface, and $x_c$ and $y_c$ are the coordinates of the particle centroid. The surface integral of the equation gives the acoustic radiation torque about the $z$ axis. The comparative surface integral values of the two terms in the above equation, i.e., $(x - x_c)$ and $(y - y_c)$ terms, dictate the positive or negative direction of the total torque acting on the particle about the $z$ axis. For the aspect ratio values, $(a/b) = 2$ and 3, we observe that the first term, i.e., the $(x - x_c)$ term, is larger than the second term, i.e., the $(y - y_c)$ term, contributing to a positive total torque acting on the body about the $z$ axis. Therefore, in these cases, an anticlockwise rotation of the particle is observed, as shown by the positive values of the orientation angle $\theta$ in Fig. 8(b). For particle aspect ratios $(a/b) = 4$ and 5, the surface integral value of the second term, i.e., the $(y - y_c)$ term, is higher than the first term, i.e., the $(x - x_c)$ term, resulting in a net negative torque and therefore clockwise rotation of the particle. Although the location of the maximum radiation force acting on the particle remains fixed, at $x_c = 138$ $\mu$m [see Fig. 8(a)], irrespective of its aspect ratio, the maximum torque acting on the particle varies along the pressure wave direction depending on the aspect ratio [Fig. 8(b)]. The variation of angular velocity with the particle position is presented in Fig. S4(b) in the Supplemental Material [46]. We observe that the particle starts rotating and attains a peak angular velocity when the torque reaches its maximum value. Interestingly, the torque acting and thereby the orientation of the particle is symmetric, i.e., equal in magnitude but opposite in direction, for aspect ratios, $(a/b) = 4$ and 5, at a location $x_{ci} = 150$ $\mu$m. The location of maximum torque shifts away from the nodal plane in the $x$ direction as $(a/b)$ increases from 2 to 3, but it shifts toward the nodal plane when $(a/b)$ increases from 4 to 5.

Now, by keeping the aspect ratio fixed, $(a/b) = 2$, we vary the volume of the particle using a scale factor $\gamma$, which defines the increase in the minor axis of the particle from its initial value, with $\gamma = 1$, 1.5, and 2. Here, $\gamma = 1$ corresponds to the initial volume of the particle, $V = 1.34 \times 10^{-16}$ m$^3$ for $(a/b) = 2$. We observe that with an increasing particle volume, the acoustic radiation force and acoustic radiation torque acting on the particle increase monotonically, as shown in Fig. 9. We observe that as the particle volume increases, the effect of the acoustic streaming field on the particle trajectory decreases, as evident from flatter trajectories for $\gamma = 1.5$ and 2, compared to a more curved trajectory for $\gamma = 1$. The particle experiences the maximum radiation force at a distance of 138 $\mu$m from the pressure nodal plane irrespective of the volume of the particle, as shown in Fig. 9(a). However, with an increase in the particle volume, the location of maximum torque acting on the particle shifts toward the pressure nodal plane [see Fig. 9(b)]. The variations of maximum
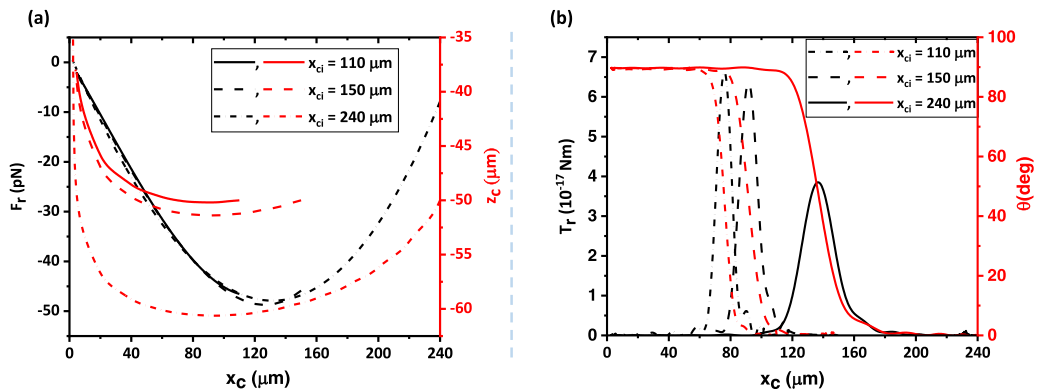
FIG. 10. (a) The $x$-$z$ trajectories of the particles and the variation in the acoustic radiation force along the $x$ coordinate of the center of the particles, for different initial positions. (b) The variation of the orientation angle and acoustic radiation torque acting on the particles with the position of the center of the particles along the $x$ direction for different initial positions. Initial orientation: MA along the $y$ direction and $\theta_i = 0°$, particle aspect ratio fixed $(a/b) = 2$, particle volume ratio fixed, $\gamma = 1$, $z_{ci} = -50 \ \mu$m.

force and torque with particle volume ratio are presented in Fig. S5(b) in the Supplemental Material [46]. The results suggest at different particle volumes that the particle translates along the $x$ direction and undergoes rotations at different positions along the $x$ direction—a larger particle rotates closer to the nodal plane, although at a much higher angular velocity (see Fig. S5(a) in the Supplemental Material [46]). This can be attributed to the increase in mass of the particle with an increase in particle volume, which increases the inertial effects, and consequently, the rotational motion of the particle gets delayed to a location closer to the nodal plane.

### 3. Effects of the initial position of the particle

The effects of the initial position of a particle along the pressure wave direction on its rotational and translational motion are studied. For a fixed initial $z$ position ($z_{ci} = -50 \ \mu$m), we observed that for a particle initially placed away from the nodal plane at a distance of 240 $\mu$m [marked by position 1 in Fig. 1(b)], the trajectory of the particle in the $x$-$z$ plane is much longer and curved more along the $z$ direction, compared to when a particle is placed at 150 and 110 $\mu$m [marked by position 2 and position 3 in Fig. 1(b)], respectively, as shown in Fig. 10(a). This is attributed to the acoustic streaming field shown in Fig. 3(b), which shows the formation of the vortices. As a result, a particle initially positioned far away from the nodal plane (i.e., a particle at position 1) follows the outer streamline of the vortices resulting in a much longer and curved trajectory compared to the particles located closer to the nodal plane (i.e., particle at position 2 and 3). Further, the motion of the particle located at positions 2 and 3 is dominated by the acoustic radiation force resulting in a flatter trajectory. The particles move toward the nodal plane due to the combined effect of acoustic radiation force and streaming-induced drag and then tend to move in the $z$ direction due to a zero acoustic radiation force at the pressure node. The curves for the variation of acoustic radiation force along the $x$ direction for different initial positions of the particle overlap, as shown in Fig. 10(a). However, the curves showing the variation of acoustic torque along the $x$ direction are markedly different, as shown in Fig. 10(b).

We observed that for a particle initially placed away from the nodal plane at a distance of 240 $\mu$m (position 1), the maximum torque acting on the particle is smaller compared to when the particle is positioned closer to the nodal plane, at a distance of 150 and 110 $\mu$m. Similarly, the maximum torque experienced by a particle initially placed at a distance of 110 $\mu$m is higher than that by a particle located at a distance of 150 $\mu$m in the $x$ direction. The distance from the nodal plane at which the torque experienced by a particle is the highest is proportional to its initial distance from
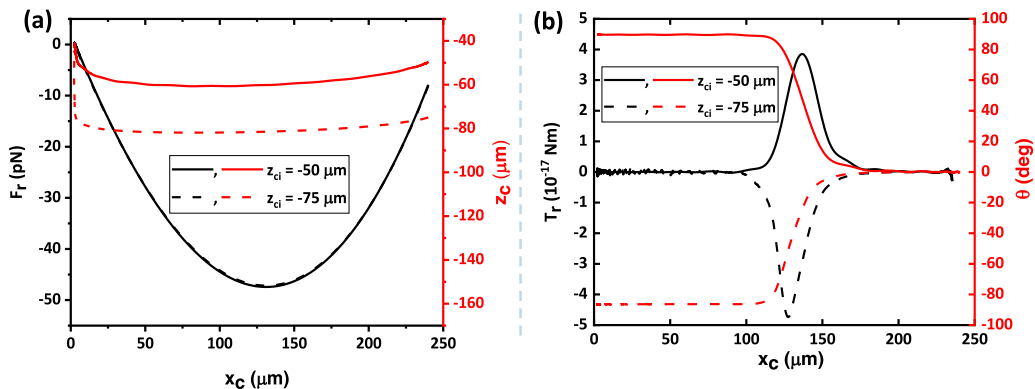
FIG. 11. (a) The $x$-$z$ trajectories of the particles (shown by red color axis) and the variation in the acoustic radiation force (shown by black color axis) along the $x$ coordinate of the center of the particles, for different initial positions along the $z$ direction. (b) The variation of the orientation angle (shown by red color axis) and acoustic radiation torque (shown by black color axis) acting on the particles with the position of the center of the particles along the $z$ direction for different initial positions. Initial orientation: MA along the $y$ direction and $\theta_i = 0°$, particle aspect ratio fixed ($\frac{a}{b} = 2$), particle volume ratio fixed, $\gamma = 1$, and $x_{ci} = 240\ \mu$m.

the nodal plane. Further, the torque profile is much sharper in the case of a particle located closer to the nodal plane than that located away from the nodal plane. Therefore, a particle located closer to the nodal plane rotates much faster compared to that located away from the nodal plane, as shown in Fig. S6(a) in the Supplemental Material [46].

The effects of the initial position of a particle in the $z$ direction ($z_{ci} = -50$ and $-75\ \mu$m) [marked by positions 1 and 4 in Fig. 3(b)] on its rotational and translational motion are studied. For a fixed $x$ position ($x_{ci} = 240\ \mu$m), we observed that the trajectories of the particle initially placed at $z_{ci} = -50$ and $-75\ \mu$m are parallel to each other until the particle reaches the pressure node [see Fig. 11(a)]. The is due to fact that the acoustic radiation force is independent of the particle position about the $z$ axis. Since the variation of the force along the $x$ axis is equal in both cases, the particle follows a similar trajectory irrespective of the initial position in the $z$ direction. It is interesting to note that, irrespective of the initial position along the $z$ direction, the particle tends to move in the $z$ direction at the pressure node which may be attributed to the acoustic streaming field. On the other hand, the particle rotates faster when it is placed at $z_{ci} = -75\ \mu$m compared to $z_{ci} = -50\ \mu$m as shown in Fig. 11(b). However, the rotation of the particle is anticlockwise when placed at $z_{ci} = -50\ \mu$m, while the rotation is clockwise when placed at $z_{ci} = -75\ \mu$m. We observed a transition in the direction of torque from positive to negative, when placed at $z_{ci} = -50\ \mu$m and $z_{ci} = -75\ \mu$m resulting in the clockwise and anticlockwise rotation. The corresponding angular velocity plot is shown in Fig. S6(b) in the Supplemental Material [46]. The time-lapse images of the particle rotational and translational motion are shown in Fig. S7 [46]. It is to be noted that a complete 90° rotation does not take place when the particle is placed at $z_{ci} = -75\ \mu$m. The streaming field is more prominent in position 4 compared to position 1 [refer to Fig. 3(b)] which may affect the particle rotation.

## IV. CONCLUSIONS

We investigated the translational and rotational motion of an oblate shaped particle exposed to bulk acoustic standing waves in a microchannel using numerical simulations. The numerical model was used to solve the acoustic and pressure fields in the microchannel and a perfectly matched layer boundary condition was used to simulate the particle dynamics. A detailed study was carried out to understand the effects of the initial orientation, aspect ratio and size, and initial location of the particle on the translational and rotational motion. We found that the acoustic streaming effects

arising from the second-order velocity fields influence the particle trajectory during its translation toward the nodal plane. Our study showed that an oblate shaped particle will rotate in order to minimize the acoustic radiation torque potential when its minor axis is not aligned with the acoustic pressure wave direction. We found the torque potential is nonzero when the particle is not aligned with the pressure wave direction and it vanishes when it is aligned. The direction of rotation of the particle was found to change from anticlockwise to clockwise beyond a critical aspect ratio, which is explained by the signs of the two competing terms in the expression of the radiation torque. The location of maximum torque and consequently rotation of the particle shifts closer to the pressure node and the magnitude of the maximum torque increases with an increase in the particle size, suggesting that a larger particle rotates faster and closer to the nodal plane. This is attributed to the increase in mass of the particle with an increase in particle volume, which increases the inertial effects and hence delays the rotation. We also find that a particle initially placed closer to the pressure node experiences a sharp increase in acoustic radiation torque and hence rotates faster. Our study illustrates the translational and rotational dynamics of an oblate shaped particle which may find relevance in understanding the dynamical behavior of an elongated micro-organism or biological cells in an acoustic field. The present model can be extended incorporating cell deformability and cell-cell interactions for predicting the behavior of a cluster of biological cells exposed to acoustic waves. Further, interaction and dynamics of nonspherical particles near a fluid-fluid interface can be analyzed numerically by coupling the present model with a multiphase flow. Such simulations will opens up a plethora of applications such as cell sorting, and medium exchange that can be explored numerically.

The data that support the findings of this study are available from the corresponding author upon reasonable request.

[1] W. Connacher, N. Zhang, A. Huang, J. Mei, S. Zhang, T. Gopesh, and J. Friend, Micro/nano acoustofluidics: Materials, phenomena, design, devices, and applications, Lab Chip **18**, 1952 (2018).

[2] H. Bruus, Acoustofluidics 7: The acoustic radiation force on small particles, Lab Chip **12**, 1014 (2012).

[3] G. T. Silva, Acoustic radiation force and torque on an absorbing compressible particle in an inviscid fluid, J. Acoust. Soc. Am. **136**, 2405 (2014).

[4] T. Hasegawa and K. Yosioka, Acoustic-radiation force on a solid elastic sphere, J. Acoust. Soc. Am. **46**, 1139 (1969).

[5] L. A. Crum, Acoustic force on a liquid droplet in an acoustic stationary wave, J. Acoust. Soc. Am. **50**, 157 (1971).

[6] M. Barmatz and P. Collas, Acoustic radiation potential on a sphere in plane, cylindrical, and spherical standing wave fields, J. Acoust. Soc. Am. **77**, 928 (1985).

[7] A. A. Doinikov, Acoustic radiation force on a spherical particle in a viscous heat-conducting fluid. I. General formula, J. Acoust. Soc. Am. **101**, 713 (1997).

[8] L. V. King, On the acoustic radiation pressure on spheres, Proc. R. Soc. London, Ser. A **147**, 212 (1934).

[9] L. P. Gor'kov, On the forces acting on a small particle in an acoustic field in an ideal fluid, Sov. Phys. Dokl. **6**, 773 (1962).

[10] M. Settnes and H. Bruus, Forces acting on a small particle in an acoustical field in a viscous fluid, Phys. Rev. E **85**, 016327 (2012).

[11] S. Z. Hoque, A. Nath, and A. K. Sen, Dynamical motion of a pair of microparticles at the acoustic pressure nodal plane under the combined effect of axial primary radiation and interparticle forces, J. Acoust. Soc. Am. **150**, 307 (2021).

[12] P. L. Marston, W. Wei, and D. B. Thiessen, Acoustic radiation force on elliptical cylinders and spheroidal objects in low frequency standing waves, in *Innovations in Nonlinear Acoustics: ISNA17–17th International Symposium on Nonlinear Acoustics Including the International Sonic Boom Forum*, AIP Conf. Proc. No. 838 (AIP, Melville, NY, 2006), p. 495.

[13] G. T. Silva and B. W. Drinkwater, Acoustic radiation force exerted on a small spheroidal rigid particle by a beam of arbitrary wavefront: Examples of traveling and standing plane waves, J. Acoust. Soc. Am. **144**, EL453 (2018).

[14] K.-M. Lim and S. Sepehrirahnama, Calculation of acoustic radiation force and moment in microfluidic devices, Int. J. Mod. Phys.: Conf. Ser. **34**, 14603809 (2014).

[15] F. B. Wijaya and K. M. Lim, Numerical calculation of acoustic radiation force and torque acting on rigid non-spherical particles, Acta Acust. Acust. **101**, 531 (2015).

[16] J. Dual, P. Hahn, I. Leibacher, D. Möller, T. Schwarz, and J. Wang, Acoustofluidics 19: Ultrasonic microrobotics in cavities: Devices and numerical simulation, Lab Chip **12**, 4010 (2012).

[17] F. Soto, E. Karshalev, F. Zhang, B. Esteban Fernandez de Avila, A. Nourhani, and J. Wang, Smart materials for microrobots, Chem. Rev. **122**, 5365 (2022).

[18] C. Chen, F. Soto, E. Karshalev, J. Li, and J. Wang, Hybrid nanovehicles: One machine, two engines, Adv. Funct. Mater. **29**, 1 (2019).

[19] J. Li, B. Esteban-Fernándezde Ávila, W. Gao, L. Zhang, and J. Wang, Micro/nanorobots for biomedicine: Delivery, surgery, sensing, and detoxification, Sci. Robot. **2**, eaam6431 (2017).

[20] S. Oberti, A. Neild, and J. Dual, Manipulation of micrometer sized particles within a micromachined fluidic device to form two-dimensional patterns using ultrasound, J. Acoust. Soc. Am. **121**, 778 (2007).

[21] B. Hammarström, N. R. Skov, K. Olofsson, H. Bruus, and M. Wiklund, Acoustic trapping based on surface displacement of resonance modes, J. Acoust. Soc. Am. **149**, 1445 (2021).

[22] P. Hahn, I. Leibacher, T. Baasch, and J. Dual, Numerical simulation of acoustofluidic manipulation by radiation forces and acoustic streaming for complex particles, Lab Chip **15**, 4302 (2015).

[23] P. Hahn, A. Lamprecht, and J. Dual, Numerical simulation of micro-particle rotation by the acoustic viscous torque, Lab Chip **16**, 4581 (2016).

[24] A. Lamprecht, T. Schwarz, J. Wang, and J. Dual, Viscous torque on spherical micro particles in two orthogonal acoustic standing wave fields, J. Acoust. Soc. Am. **138**, 23 (2015).

[25] J. P. Leão-Neto, J. H. Lopez, and G. T. Silva, Acoustic radiation torque exerted on a subwavelength spheroidal particle by a travelling and standing plane wave, J. Acoust. Soc. Am. **147**, 2177 (2020).

[26] T. Schwarz, G. Petit-Pierre, and J. Dual, Rotation of non-spherical micro-particles by amplitude modulation of superimposed orthogonal ultrasonic modes, J. Acoust. Soc. Am. **133**, 1260 (2013).

[27] A. Garbin, I. Leibacher, P. Hahn, H. Le Ferrand, A. Studart, and J. Dual, Acoustophoresis of disk-shaped microparticles: A numerical and experimental study of acoustic radiation forces and torques, J. Acoust. Soc. Am. **138**, 2759 (2015).

[28] O. Jakobsson, M. Antfolk, and T. Laurell, Continuous flow two-dimensional acoustic orientation of nonspherical cells, Anal. Chem. **86**, 6111 (2014).

[29] P. Hahn and J. Dual, A numerically efficient damping model for acoustic resonances in microfluidic cavities, Phys. Fluids **27**, 062005 (2015).

[30] H. Bruus, Acoustofluidics 2: Perturbation theory and ultrasound resonance modes, Lab Chip **12**, 20 (2012).

[31] S. Z. Hoque and A. K. Sen, Interparticle acoustic radiation force between a pair of spherical particles in a liquid exposed to a standing bulk acoustic wave, Phys. Fluids **32**, 072004 (2020).

[32] *Acoustics Module User's Guide*, COMSOL MULTIPHYSICS® v. 5.3, COMSOL AB, Stockholm, Sweden, 2017, pp. 134–137.

[33] R. Habibi, C. Devendran, and A. Neild, Trapping and patterning of large particles and cells in a 1D ultrasonic standing wave, Lab Chip **17**, 3279 (2017).

[34] S. Karthick and A. K. Sen, Improved understanding of the acoustophoretic focusing of dense suspensions in a microchannel, Phys. Rev. E **96**, 052606 (2017).

[35] S. Karthick and A. K. Sen, Improved Understanding of Acoustophoresis and Development of an Acoustofluidic Device for Blood Plasma Separation, Phys. Rev. Appl. **10**, 034037 (2018).

[36] S. Karthick, P. N. Pradeep, P. Kanchana, and A. K. Sen, Acoustic impedance-based size-independent isolation of circulating tumour cells from blood using acoustophoresis, Lab Chip **18**, 3802 (2018).

[37] E. Hemachandran, T. Laurell, and A. K. Sen, Continuous Droplet Coalescence in a Microchannel Coflow Using Bulk Acoustic Waves, Phys. Rev. Appl. **12**, 044008 (2019).

[38] A. Nath and A. K. Sen, Acoustic Behavior of a Dense Suspension in an Inhomogeneous Flow in a Microchannel, Phys. Rev. Appl. **12**, 054009 (2019).

[39] J. T. Karlsen and H. Bruus, Forces acting on a small particle in an acoustical field in a thermoviscous fluid, Phys. Rev. E. **92**, 043010 (2015).

[40] A. Tahmasebipour, L. Friedrich, M. Begley, H. Bruus, and C. Meinhart, Toward optimal acoustophoretic microparticle manipulation by exploiting asymmetry, J. Acoust. Soc. Am. **148**, 359 (2020).

[41] P. Hahn, O. Schwab, and J. Dual, Modeling and optimization of acoustofluidic micro-devices, Lab Chip **14**, 3937 (2014).

[42] M. A. Hopcroft, W. D. Nix, and T. W. Kenny, What is the Young's modulus of silicon?, J. Microelectromech. Syst. **19**, 229 (2010).

[43] J. Lei, P. Glynne-Jones, and M. Hill, Acoustic streaming in the transducer plane in ultrasonic particle manipulation devices, Lab Chip **13**, 2133 (2013).

[44] W. L. Nyborg, Acoustic streaming due to attenuated plane waves, J. Acoust. Soc. Am. **25**, 68 (1953).

[45] J. Lei, M. Hill, and P. Glynne-Jones, Numerical simulation of 3D boundary-driven acoustic streaming in microfluidic devices, Lab Chip **14**, 532 (2014).

[46] See Supplemental Material at http://link.aps.org/supplemental/10.1103/PhysRevFluids.7.114204 for the hydrodynamic resistance matrix, effects of initial orientation on the dynamics of an oblate shaped particle, dynamical motion of an oblate shaped particle, and angular velocity variation. Video S1: z rotation, Video S2: y rotation, Video S3: nonrotation.

[47] P. Glynne-Jones, P. P. Mishra, R. J. Boltryk, and M. Hill, Efficient finite element modeling of radiation forces on elastic particles of arbitrary size and geometry, J. Acoust. Soc. Am. **133**, 1885 (2013).

[48] S. M. Zareei, S. Sepehrirahnama, M. Jamshidian, and S. Ziaei-Rad, Three-dimensional numerical simulation of particle acoustophoresis: COMSOL implementation and case studies, Eng. Comput. (2022).

[49] T. Hasegawa, Acoustic radiation force on a sphere in a quasistationary wave field—theory, J. Acoust. Soc. Am. **65**, 32 (1979).

[50] P. L. Marston, Phase-shift expansions for approximate radiation forces on solid spheres in inviscid-acoustic standing waves, J. Acoust. Soc. Am. **142**, 3358 (2017).